Supplementary Materials

The Touch-Code Glove: a multimodal mapping interface with triboelectric-digital encoding for intuitive robot training

Yuyang Sun, Dongsheng Li, Ruxiao Yang, Zhicun Zhou, Tianci Ji, Bo Lu, Lining Sun, Huicong Liu*

School of Mechanical and Electrical Engineering, Jiangsu Key Laboratory of Embodied Intelligence Robot Technology, Soochow University, Suzhou 215137, Jiangsu, China.

***Correspondence to:** Prof. Huicong Liu, School of Mechanical and Electrical Engineering, Jiangsu Key Laboratory of Embodied Intelligence Robot Technology, Soochow University, Suzhou 215137, Jiangsu, China. E-mail: hcliu078@suda.edu.cn

This file includes:

Supplementary Texts

Text 1. Electrostatic simulation and signal coupling in multi-point touch interactions.
Text 2. COMSOL simulation and parametric analysis of geometric effects on triboelectric performance.
Text 3. Structural framework for CNN-LSTM model.
Text 4. Additional validation of CNN-LSTM through dataset scaling and cross-user experiments.
Text 5. Conflict-resolution strategy for multi-point coupling in the Wrist-pad.
Text 6. Analysis of resistance changes in the hydrogel during deformation.
Text 7. Calculation and analysis of the limit of detection (LOD) for the Wrist-pad.
Text 8. Long-term stability and environmental durability evaluation.
Text 9. Stability of hydrogel-based finger bending sensors in dry environments.
Text 10. Structural framework for 1D-CNN.
Text 11. Multi-user generalization of CNN-LSTM and 1D-CNN models.
Text 12. Touch-to-path mapping strategy based on triboelectric touch inputs.
Text 13. Signal acquisition circuitry for strain and triboelectric sensing in the Touch-Code glove.
Text 14. Ergonomic evaluation of the glove prototype.

Supplementary Figures

Figure 1. Fabrication process of the Finger-fiber.
Figure 2. Fabrication process of the Wrist-pad.
Figure 3. Structural integration of the multimodal sensors in the glove.
Figure 4. Schematic of the components of the Touch-Code Glove.
Figure 5. Schematic explanation of positive and negative resistance changes of the hydrogel element during wrist flexion and extension.
Figure 6. Electrostatic simulation of different coupled triboelectric pairs.
Figure 7. COMSOL electrostatic simulations showing the potential difference distribution on the triboelectric contact surface with varying hemispherical heights (h).
Figure 8. COMSOL electrostatic simulations showing the potential difference distribution on the triboelectric contact surface with varying hemispherical radii (R).
Figure 9. Parametric analysis results showing the variation of peak-to-peak voltage ($_{pp}$)

as a function of hemispherical height (h) and radius (R).
Figure 10. Structural framework for CNN-LSTM model.
Figure 11. Confusion matrices of classification results under different training sample sizes.
Figure 12. Confusion matrices of classification results using the new multi-user testing dataset.
Figure 13. Conflict-resolution strategy for multi-point coupling in the Wrist-pad.
Figure 14. The raw resistance change collected over 5 seconds with no applied bending.
Figure 15. Sensitivity variation over 14 days under different temperatures at 70% RH.
Figure 16. Sensitivity variation over 14 days under different humidity levels at 25 °C.
Figure 17. Hysteresis ratio variation over 14 days under different temperatures at 70% RH.
Figure 18. Hysteresis ratio variation over 14 days under different humidity levels at 25 °C.
Figure 19. Repetitive bending tests of Finger-fiber under different humidity conditions.
Figure 20. Reproducibility and long-term durability of the Finger-fiber.
Figure 21. Structural framework for 1D-CNN.
Figure 22. Confusion matrices of classification results using the new multi-user testing dataset.
Figure 23. Confusion matrices of classification results using the new multi-user testing dataset. “G” indicates “gesture”.
Figure 24. Touch-based path programming via triboelectric touch commands on the Wrist-pad.
Figure 25. Response of the triboelectric Wrist-pad under prolonged pressing and sequential gestures.
Figure 26. Signal acquisition circuits for resistive and triboelectric sensing.
Figure 27. Verification of noise suppression for the Touch-Code Glove.
Figure 28. Mechanical flexibility of the glove prototype.
Figure 29. Ergonomic performance during long-term wearing.

Supplementary Tables

Table 1. Parameters of the CNN-LSTM network structure.
Table 2. Classification accuracies under different training sample sizes.
Table 3. Classification accuracies of different modes using the new multi-user testing

dataset.
Table 4. Comparison between representative studies and the Touch-Code Glove.
Table 5. Parameters of the 1D-CNN structure.
Table 6. Classification accuracies for different modes using the new multi-user testing dataset.
Table 7. Classification accuracies of different gestures using the new multi-user testing dataset.

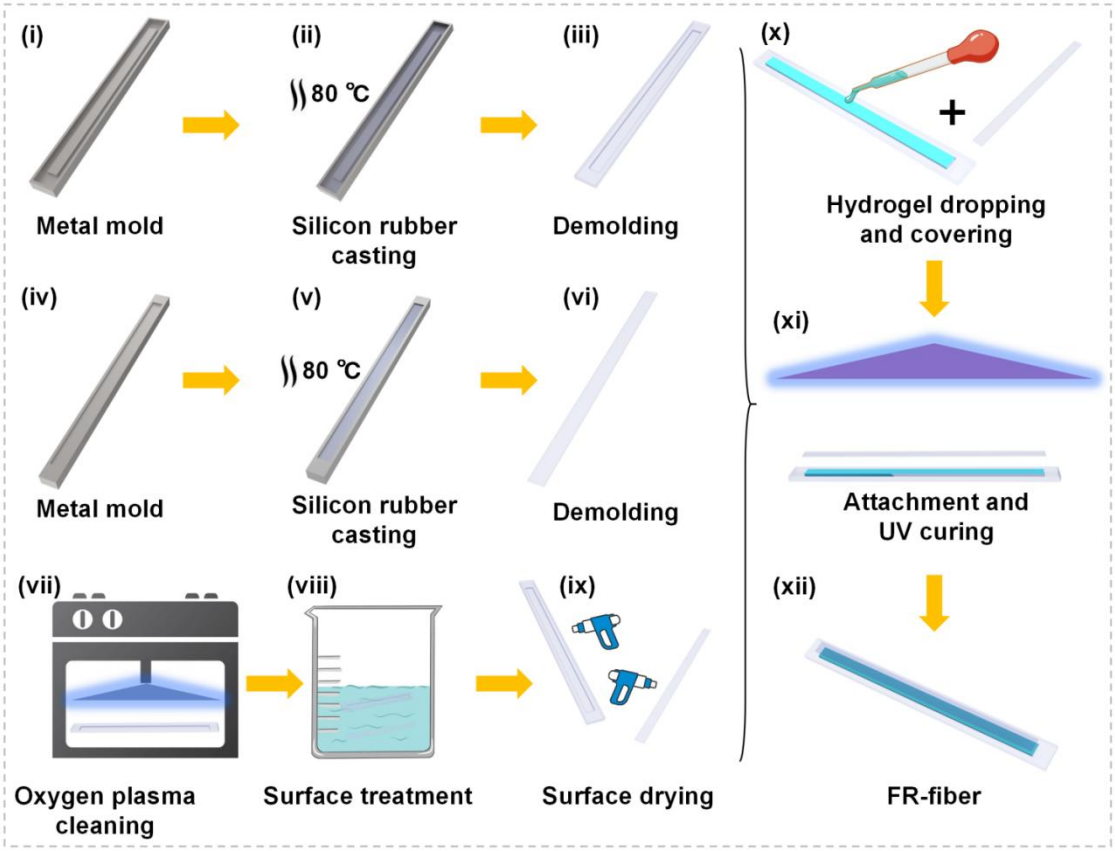

Supplementary Figure 1. Fabrication process of the Finger-fiber.

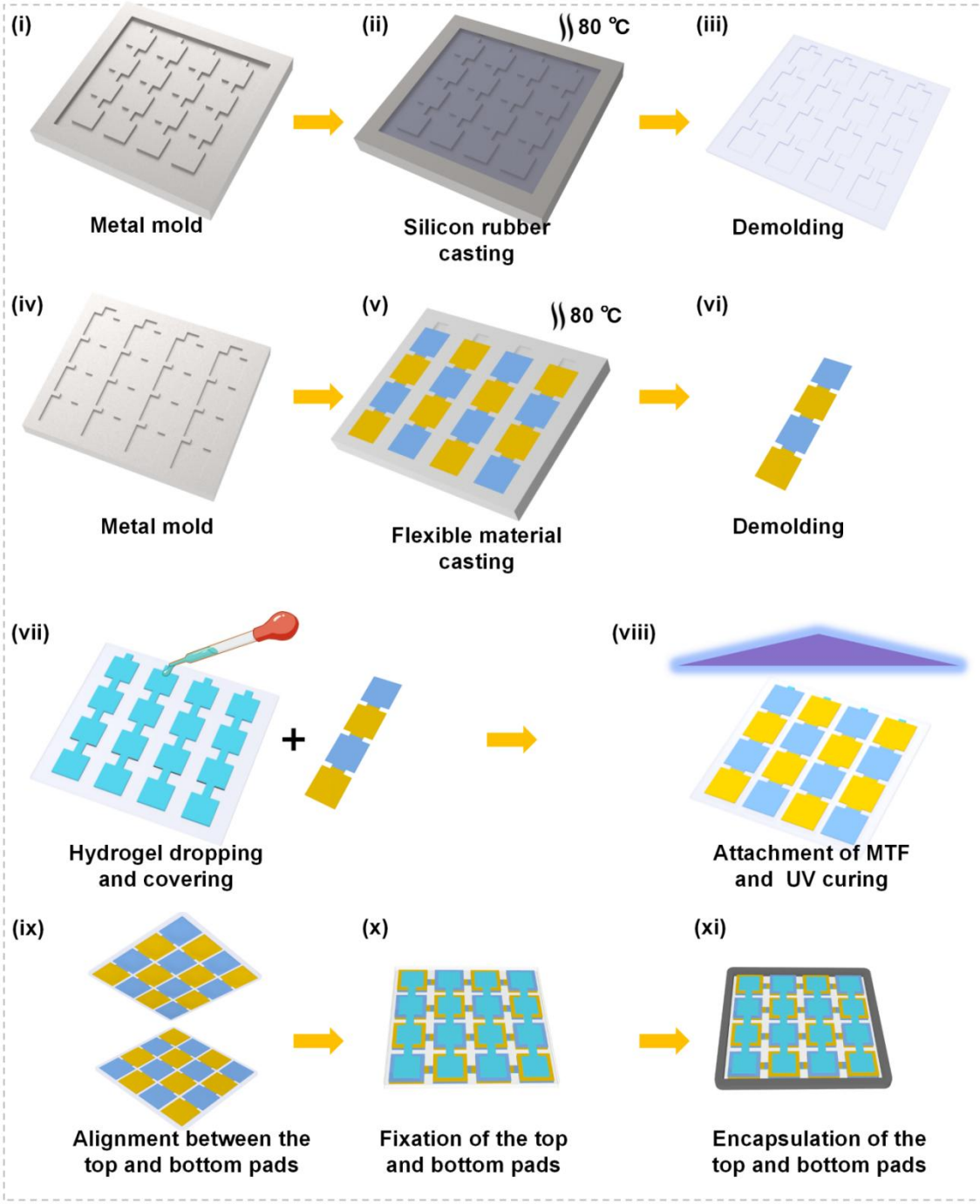

Supplementary Figure 2. Fabrication process of the Wrist-pad.

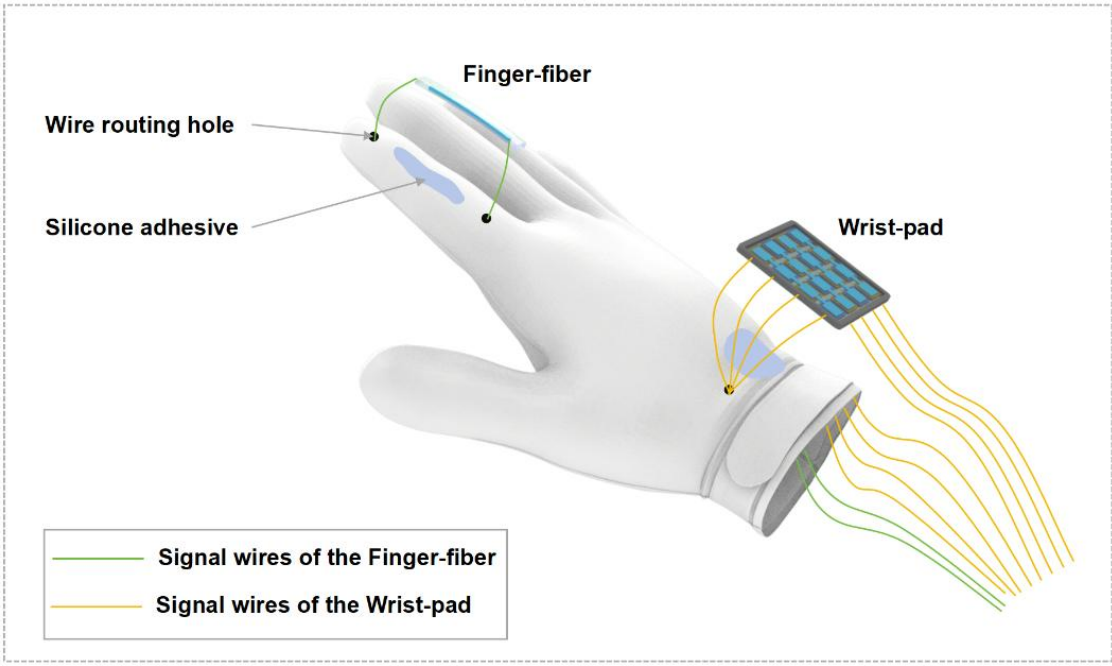

Supplementary Figure 3. Structural integration of the multimodal sensors in the glove.

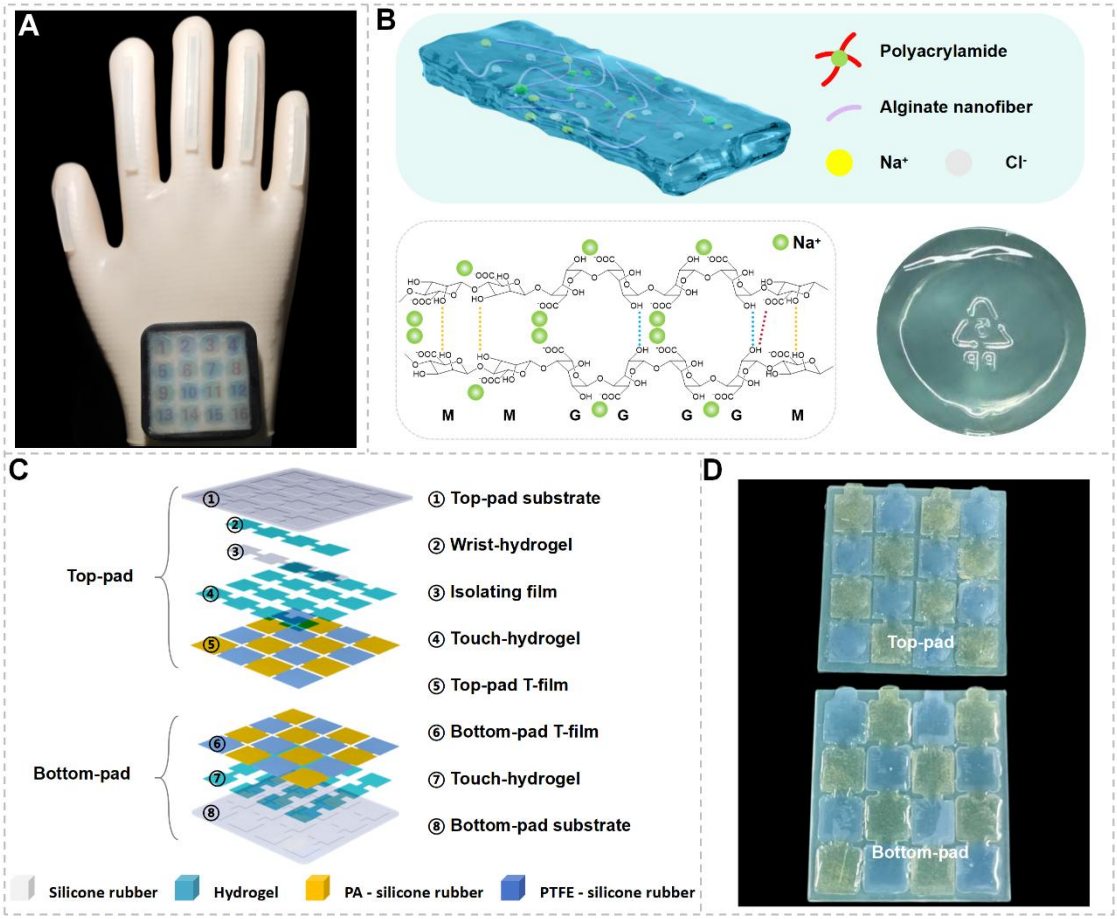

Supplementary Figure 4. Schematic of the components of the Touch-Code Glove. (A) Schematic of the Touch-Code Glove; (B) Schematic structure, molecular formula, and transparency of the hydrogel; (C) Schematic structure of the Wrist-pad; (D) Schematic of the unfolded Wrist-pad structure.

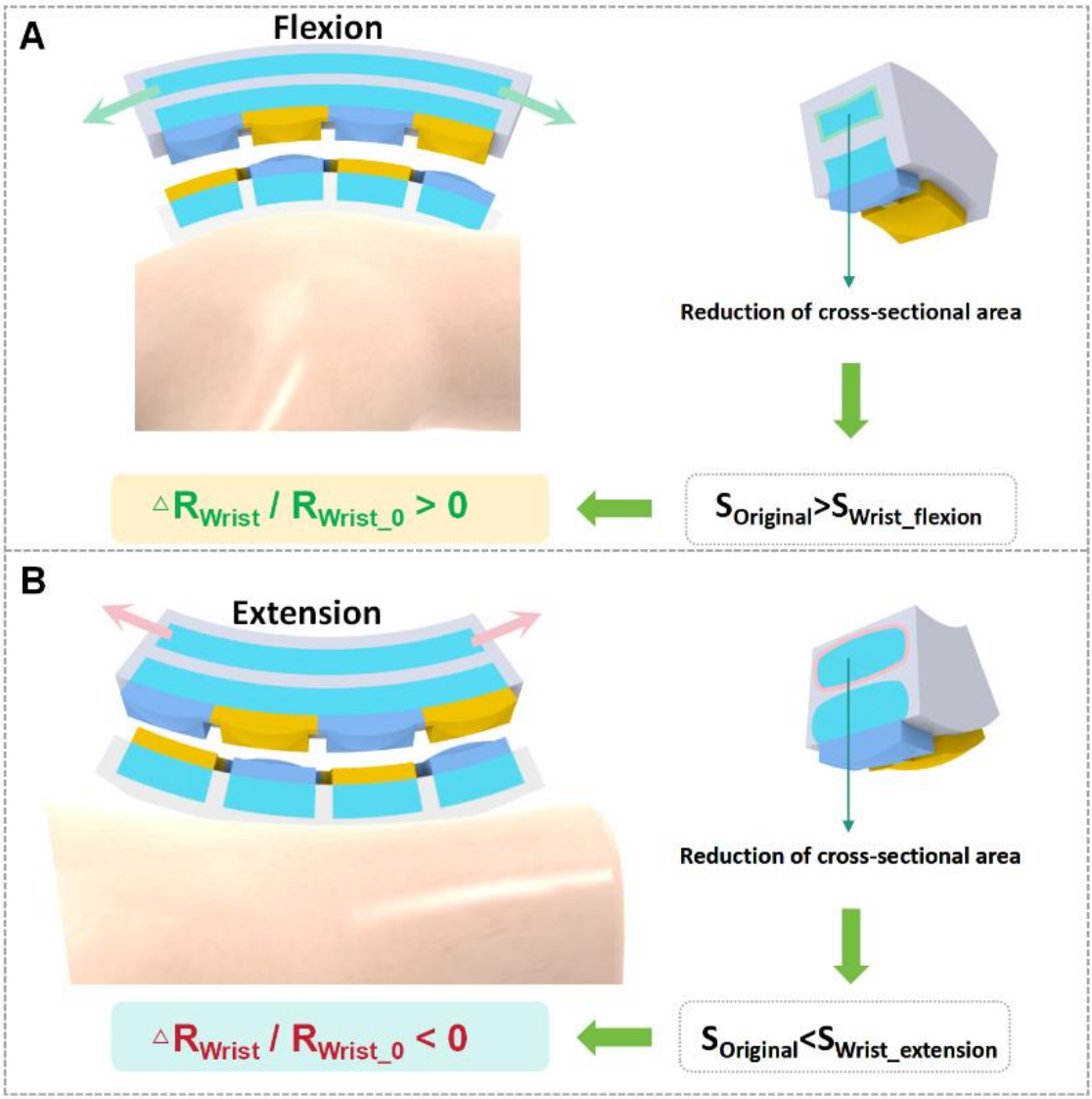

Supplementary Figure 5. Schematic explanation of positive and negative resistance changes of the hydrogel element during wrist flexion and extension. (A) Wrist flexion: Flexion compresses the hydrogel element, reducing its effective cross-sectional area. This leads to an increase in resistance; (B) Wrist extension: Extension stretches the hydrogel element, enlarging its effective cross-sectional area. This results in a decrease in resistance.

Supplementary Text 1. Electrostatic simulation and signal coupling in multi-point touch interactions.

While the digital encoding strategy is highly effective for discrete, well-separated touch events, a more intricate challenge emerges during dense, multi-point interactions: signal coupling. To elucidate the electrostatic induction that arises between triboelectric surfaces with different properties, finite element simulations (COMSOL) were conducted to analyze the potential distribution at a coupled touch point composed of PA-silicone rubber (regions ①) and PTFE-silicone rubber (regions ②). The simulation was performed at four different separation distances (D = 5 mm, 4 mm, 3 mm, and 2 mm) to capture the evolution of electrostatic interaction during approach. When the separation is 5 mm, the induced potential difference between the two material groups reaches its maximum. As the distance decreases, the potential gradually redistributes and weakens, driving free electrons to flow between the electrode and the ground, thereby generating an alternating current signal. Notably, each triboelectric surface exhibits distinct local potential induced by the presence of its counterpart with opposite polarity, and the central region between the opposing surfaces consistently exhibits a zero-potential zone. This indicates that when electrostatic induction occurs between adjacent triboelectric layers, the induced charges remain localized without drifting between the surfaces, highlighting the spatially confined nature of the triboelectric charge distribution. Figure 6 illustrates single-, triple-, and quadruple-pair coupled touch configurations. Electrostatic simulations show that each pair maintains its expected potential variation during contact-separation, and the junction regions consistently remain at zero potential.

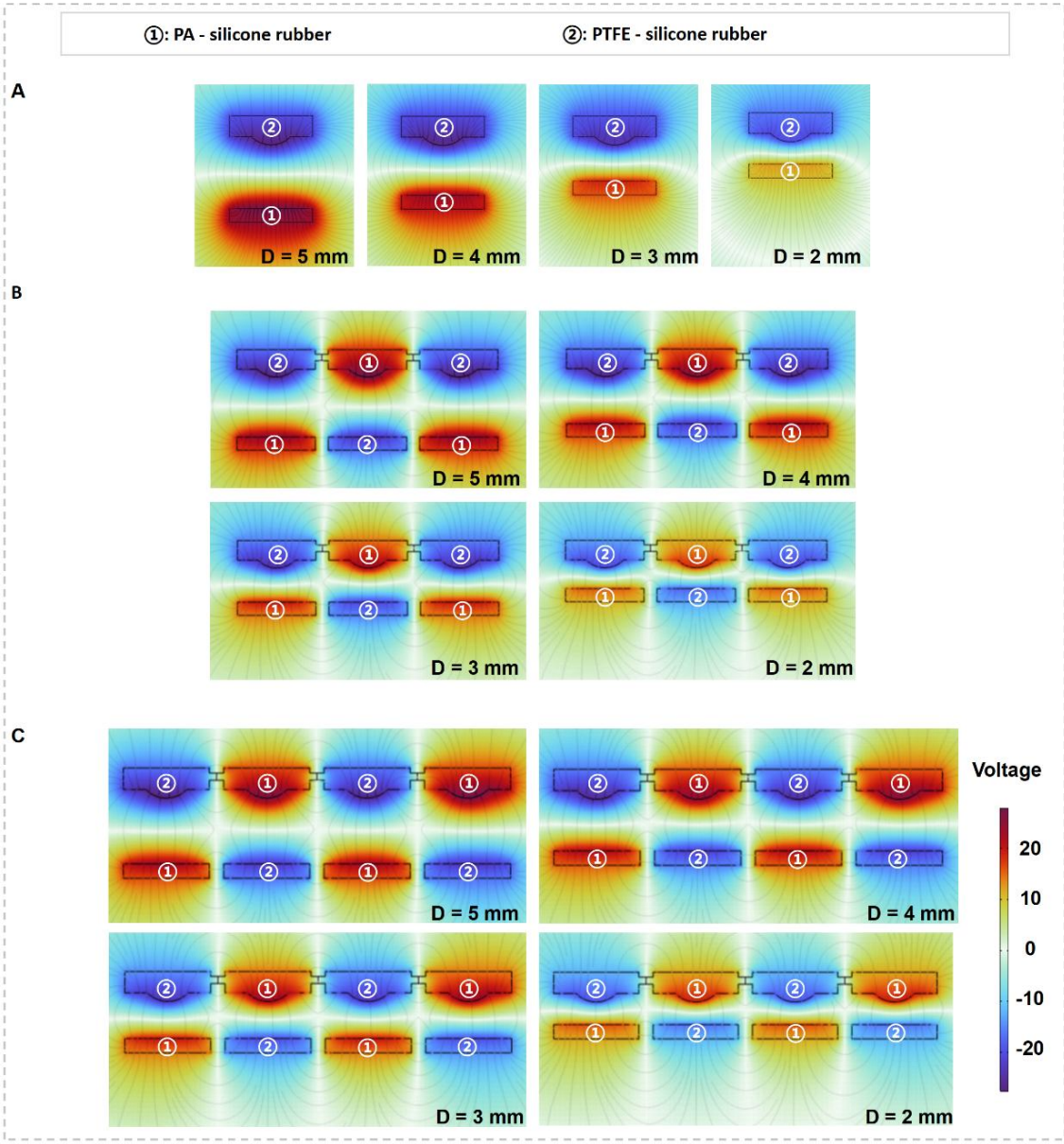

Supplementary Figure 6. Electrostatic simulation of different coupled triboelectric pairs. (A) Electrostatic simulation of single-triboelectric pair; (B) Electrostatic simulation of triple-triboelectric pair; (C) Electrostatic simulation of quadruple-triboelectric pair.

Supplementary Text 2. COMSOL simulation and parametric analysis of geometric effects on triboelectric performance.

COMSOL electrostatic simulations (Figures 7-9) reveal that geometric parameters, height (h) and radius (R), directly affect potential distribution and charge transfer. Increasing h enhances local deformation and surface potential difference, with an optimal value at ~0.5 mm before stress dispersion reduces stability. Enlarging R initially increases contact area and V_{pp}, but excessive R leads to uniform pressure and reduced charge density, with the optimal range at ~1.3-1.7 mm. These results confirm that optimized contact mechanics and potential distribution improve sensitivity and signal-to-noise ratio (SNR), providing guidelines for structural design.

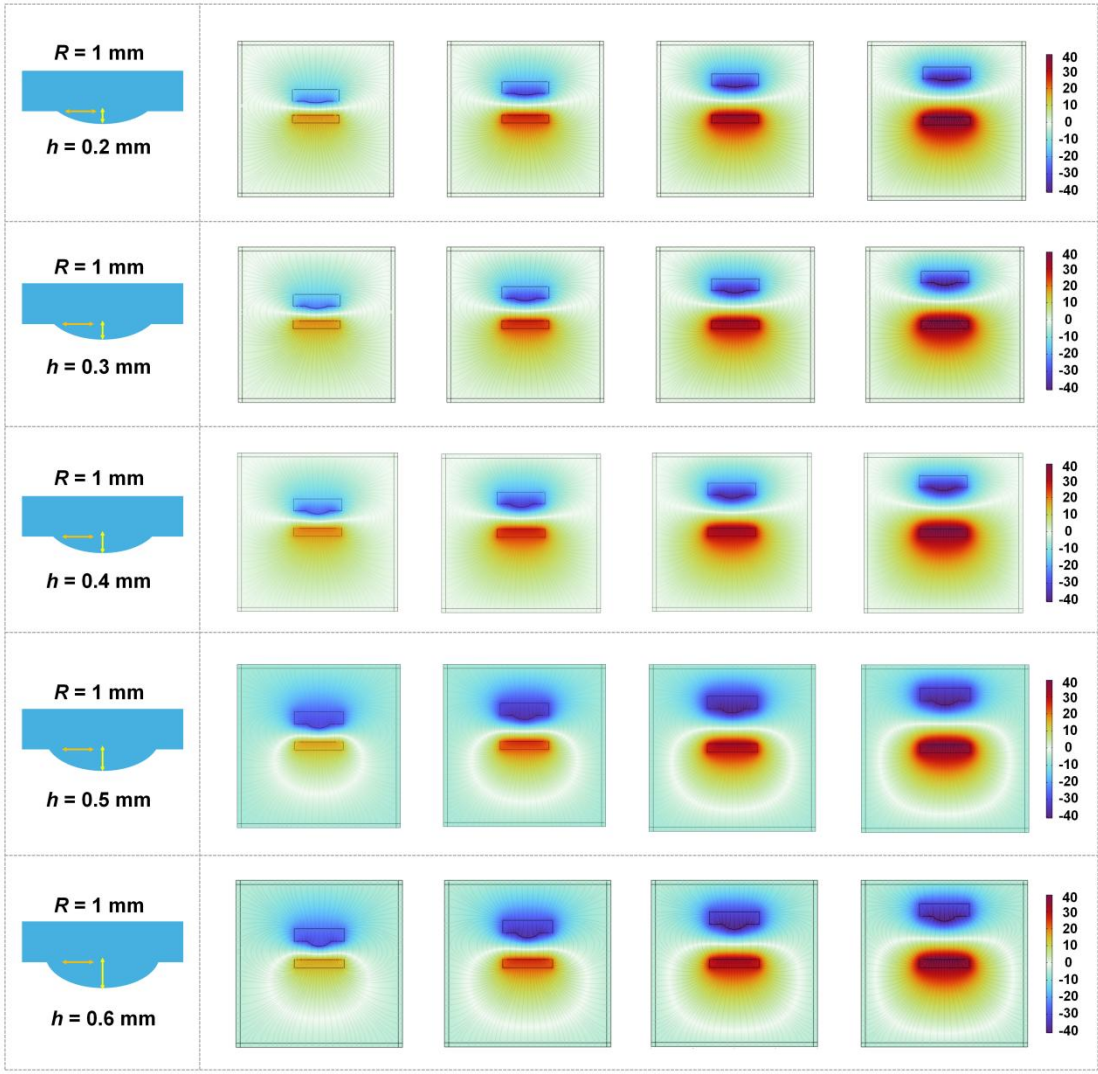

Supplementary Figure 7. COMSOL electrostatic simulations showing the potential difference distribution on the triboelectric contact surface with varying hemispherical heights (*h*).

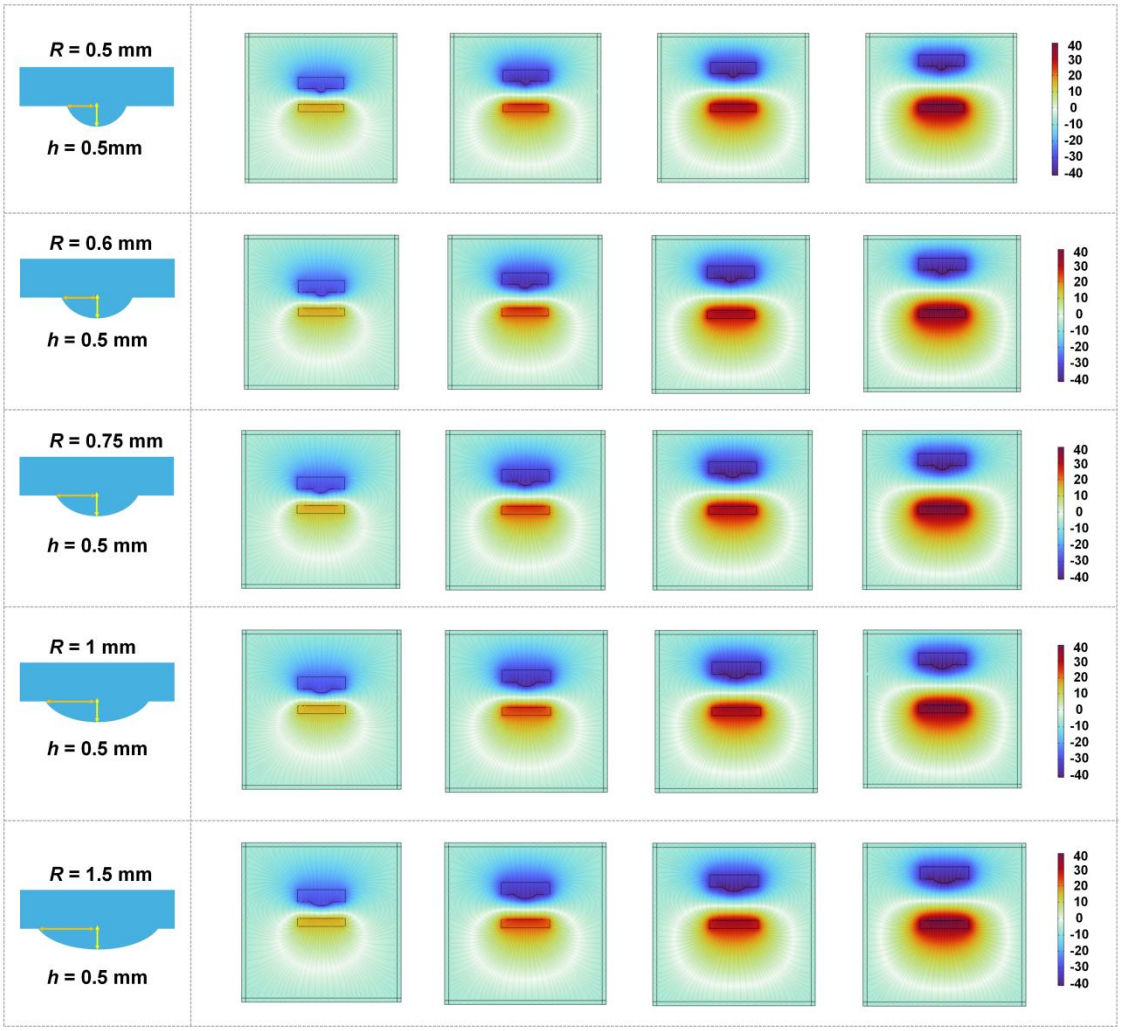

Supplementary Figure 8. COMSOL electrostatic simulations showing the potential difference distribution on the triboelectric contact surface with varying hemispherical radii (*R*).

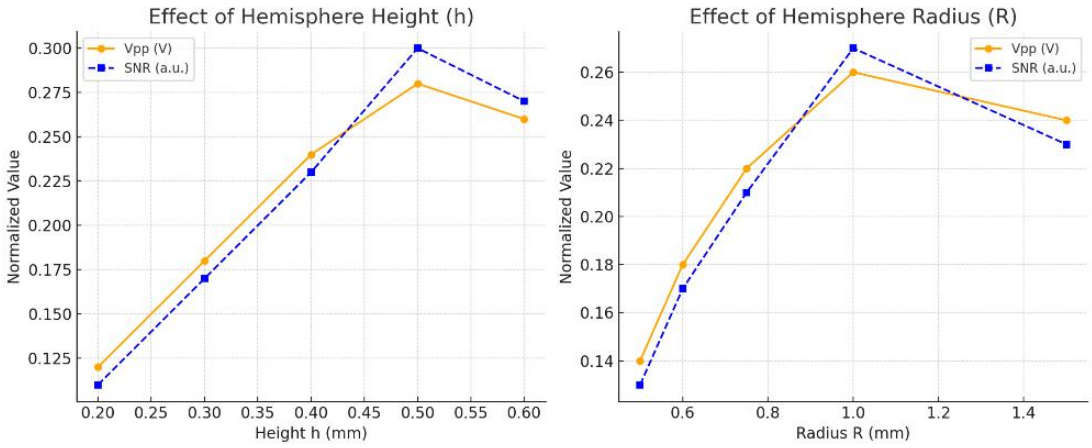

Supplementary Figure 9. Parametric analysis results showing the variation of peak-to-peak voltage (V_{pp}) as a function of hemispherical height (h) and radius (R).

Supplementary Text 3. Structural framework for CNN-LSTM model.

To effectively capture both local and temporal features from multi-channel time-series signals, a convolutional neural network (CNN)-long short-term memory (LSTM) model was constructed, as displayed in Figure 10. This network accepts an input of size 8×200, representing eight-channel signals over 200 time steps. The convolutional front-end consists of four one-dimensional convolutional layers, each employing a kernel size of 3 and a stride of 1. To preserve the temporal resolution throughout the convolutional blocks, a "same" padding scheme is applied to all convolutional layers, ensuring that the output length remains constant to the input. A max-pooling layer with a pooling size of 2 is inserted after the first convolutional layer, reducing the temporal dimension to 100. The resulting feature map is then transposed to match the expected input format of the LSTM layer, where a single-layer LSTM with 64 hidden units models long-term temporal dependencies. The output of the LSTM is flattened into a one-dimensional feature vector and passed through three fully connected layers, culminating in a four-class softmax classifier. This architecture balances efficient local feature extraction and temporal modeling while maintaining structural alignment via consistent temporal dimensions across the convolutional stages.

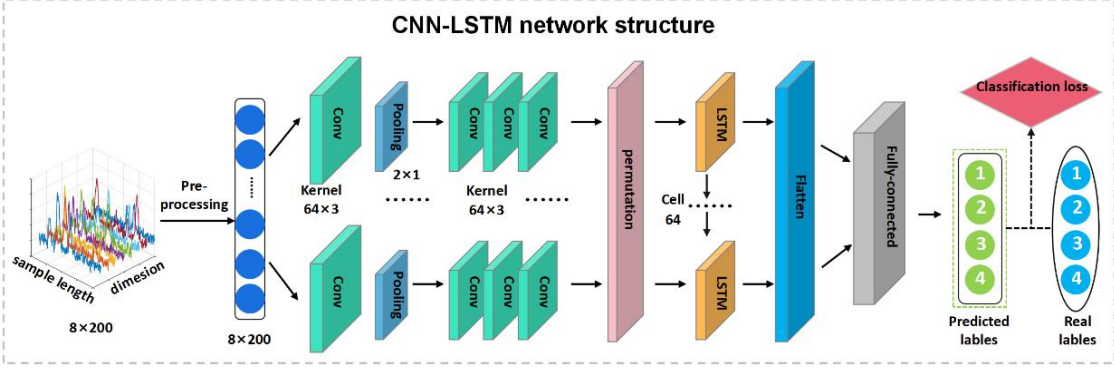

Supplementary Figure 10. Structural framework for CNN-LSTM model.

Supplementary Table 1. Parameters of the CNN-LSTM network structure

Network layer	Parameter	Activation function	Output size
Input	/	/	8×200
Convolutional layer	Stride = 1; Kernel size = 3; Channel number = 64;	ReLU	64×200
Pooling Layer	Max Pooling Size = 2	/	64×100
Convolutional layer	Stride = 1; Kernel size = 3; Channel number = 64;	ReLU	64×100
Convolutional layer	Stride = 1; Kernel size = 3; Channel number = 64;	ReLU	64×100
Convolutional layer	Stride = 1; Kernel size = 3; Channel number = 64;	ReLU	64×100
Permute	Swap from (64×100) → (100×64)	/	100×64
LSTM layer	Cell size = 64	/	100×64
Flatten	/	/	1×6400
F1	Weight = 6400×128; Bias = 128	ReLU	1×128
F2	Weight = 128×64; Bias = 64	ReLU	1×64
F3	Weight = 64×4; Bias = 4	Softmax	1×4

Supplementary Text 4. Additional validation of CNN-LSTM through dataset scaling and cross-user experiments.

To further validate the CNN-LSTM, two additional experiments were conducted.

First, the training dataset size was varied from 50 to 1,000 samples per class to examine the effect of data availability. As summarized in Table 2 and Figure 11, accuracy increased steadily with larger datasets. Even with only 50 samples, the model achieved 75.0%, indicating meaningful pattern extraction. Accuracy rose to 89.4% with 100 samples and reached 94.7% with 200 samples. At 500 and 1,000 samples, performance nearly saturated at 97.7% and 98.4%, demonstrating strong reliability once sufficient data is provided.

Second, cross-user generalization was tested with 10 volunteers whose palm widths ranged from 15 cm to 21 cm. Each participant contributed 50 samples per mode, yielding a total of 2000 triboelectric samples. The CNN-LSTM consistently maintained accuracies above 91% across all modes, despite minor reductions due to inter-user variability. Together, these results confirm that the CNN-LSTM is both scalable with respect to dataset size and robust across diverse users, providing solid evidence of its practical applicability in real-world tasks (Table 3 and Figure 12).

Supplementary Table 2. Classification accuracies under different training sample sizes.

Dataset size		50	100	200	500	1000
Classification Accuracy (%)	Mode 1	76.3	89.2	95.8	98.1	99.2
	Mode 2	74.7	89.7	94.1	97.8	98.3
	Mode 3	72.9	89.3	94.8	97.5	98.0
	Mode 4	75.9	89.6	94.3	97.4	98.3
	average	75.0	89.4	94.7	97.7	98.4

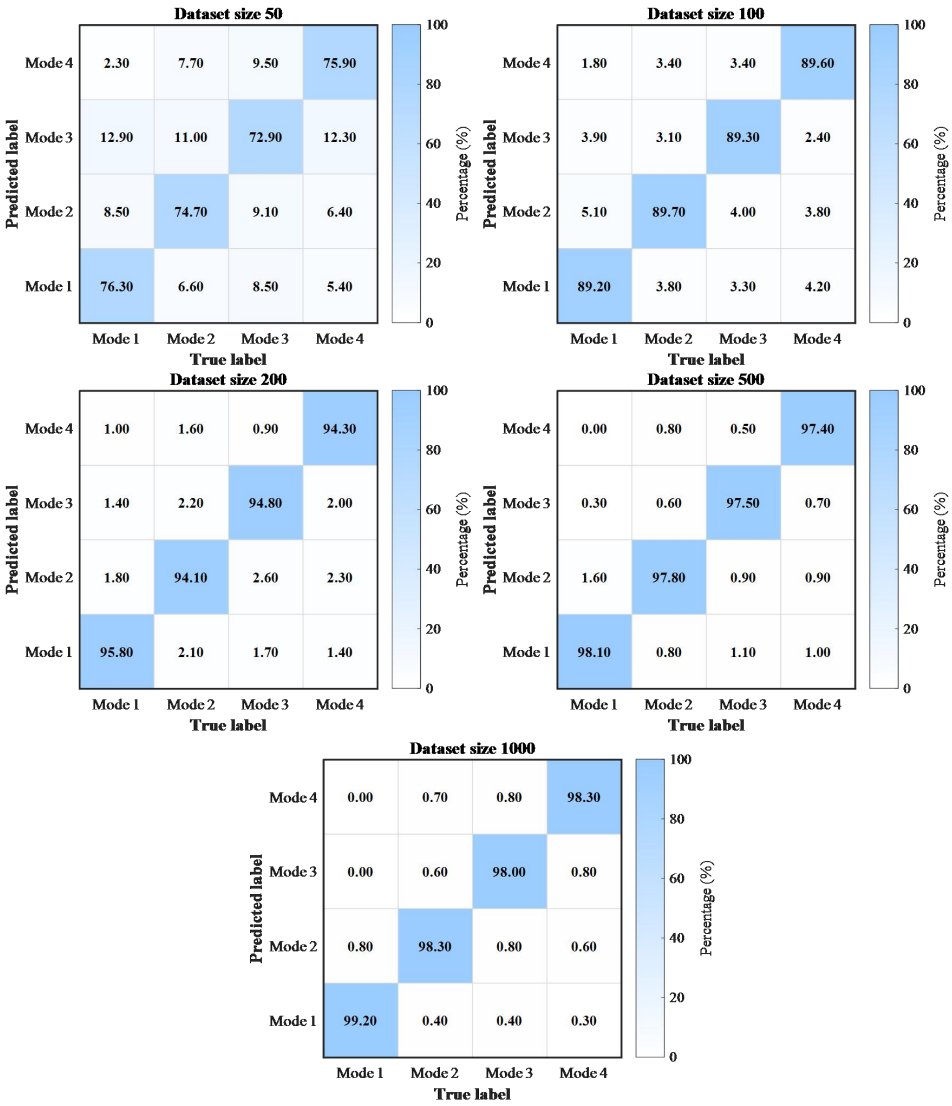

Supplementary Figure 11. Confusion matrices of classification results under different training sample sizes.

Supplementary Table 3. Classification accuracies of different modes using the new multi-user testing dataset.

Mode category	Mode 1	Mode 2	Mode 3	Mode 4
Classification accuracy (%)	91.6	96.0	92.0	94.4

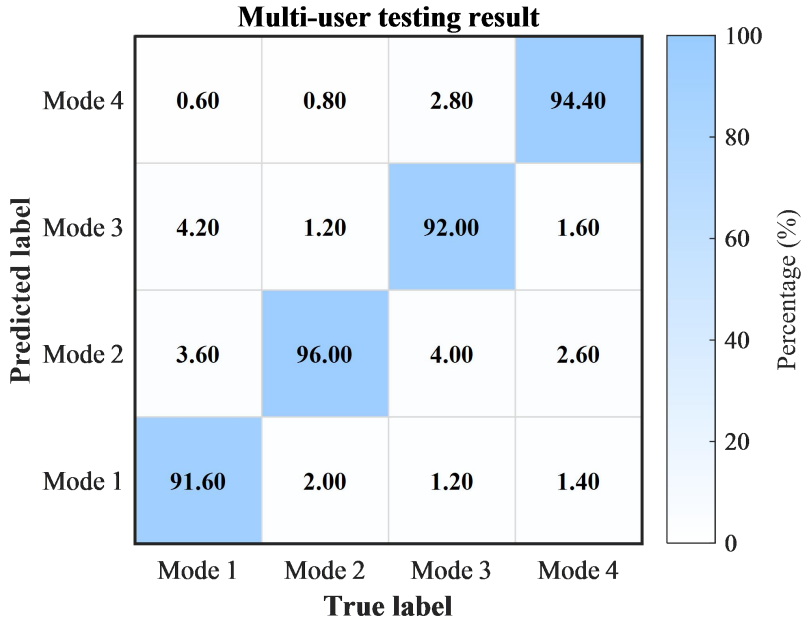

Supplementary Figure 12. Confusion matrices of classification results using the new multi-user testing dataset.

Supplementary Text 5. Conflict-resolution strategy for multi-point coupling in the Wrist-pad.

Figure 13 illustrates three representative cases. As shown in Figure 13A, when P6 and P7 are simultaneously touched, channels with zero signals (C1, C4, C5, C7, and C8) are first excluded, leaving active channels C2, C3, and C6. Since C2 and C3 belong to the same vertical type, C6 is identified as the coupled channel. If its waveform exhibits complex or partially canceled features, the CNN-LSTM trained on such scenarios can correctly recognize C6 as a coupled signal and resolve the two touch points. The same principle applies to Figure 13B and 13C, where nonresponsive channels are excluded first, followed by waveform interpretation. This combined rule-based exclusion and learning-based recognition enables robust resolution of multi-point coupling and prevents false triggers. Recognition accuracy of the CNN-LSTM framework exceeded 98% across all gesture categories, confirming the effectiveness of the approach.

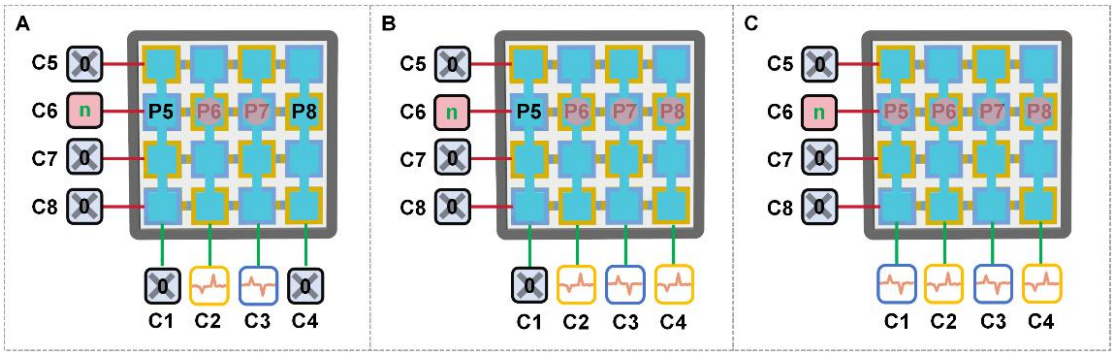

Supplementary Figure 13. Conflict-resolution strategy for multi-point coupling in the Wrist-pad. (A) Two-point simultaneous touch case; (B) Three-point simultaneous touch case; (C) Four-point simultaneous touch case.

Supplementary Text 6. Analysis of resistance changes in the hydrogel during deformation.

When bent, the Finger-fiber stretches and functions as a strain-resistive sensor governed by Ohm's Law. The relationship between relative resistance change and strain can be derived by considering the reduction of cross-sectional area (*A*-*A*) during stretching, as expressed by

Initial resistance:

$$R_0 = \frac{\rho \cdot L_0}{A_0} \tag{1}$$

The resistance of the FR-fiber when stretched to a length of L_1 is:

$$R_1 = \frac{\rho \cdot L_1}{A_1} \tag{2}$$

where ρ is the resistivity of the Finger-hydrogel, L_0 and L_1 are the lengths of the Finger-fiber before and after stretching, and A_0 and A_1 are the cross-sectional areas of the Finger-fiber before and after stretching. The volume V of the Finger-hydrogel can be considered unchanged before and after stretching, therefore：

$$V = L_0 \cdot A_0 = L_1 \cdot A_1 \tag{3}$$

Substituting formula (3) into formula (2), we obtain

$$R_1 = \frac{\rho \cdot L_1^{\,2}}{A_0 L_0} \tag{4}$$

According to the definition of stretching, we obtain:

$$\varepsilon = \frac{L_1 - L_0}{L_0} \tag{5}$$

By combining formulas (4) and (5), the relationship between the rate of resistance change and the strain can be obtained, i.e.:

$$\frac{\Delta R}{R_0} = \frac{R_1}{R_0} - 1 = \left(\frac{L_1}{L_0}\right)^2 - 1 = \varepsilon^2 + 2\varepsilon \tag{6}$$

From the above analysis, the relative resistance change rate increases under stretching and decreases under compression of the Finger-fiber.

Supplementary Text 7. Calculation and analysis of the limit of detection (LOD) for the Wrist-pad.

Figure 14 presents the raw resistance change ($\Delta R/R_0$) collected over five seconds with no applied bending. The signal fluctuates randomly around zero without drift, reflecting the intrinsic noise of the sensor. The standard deviation of the noise (σ_noise) was calculated to be approximately 0.0026%. Based on the strain-angle calibration shown in Figure 4A(ii), the fitted slopes for wrist flexion and extension are ~-0.098 %·deg^{-1} and ~0.099 %·deg^{-1}, respectively. The strain sensitivity (s) can therefore be expressed as:

$$s = \frac{\Delta R / R_0}{\Delta \theta} (\% \deg^{-1})$$

Thus, the minimum detectable angle change (limit of detection, LOD) can be derived as:

$$LOD = \frac{\sigma_{noise}}{s}$$

Substituting the values:

For wrist flexion:

$$LOD = \frac{0.0026}{0.098} \approx 0.026°$$

For wrist flexion:

$$LOD = \frac{0.0026}{0.098} \approx 0.026°$$

These results demonstrate that the system achieves an ultralow limit of detection of ~0.03°.

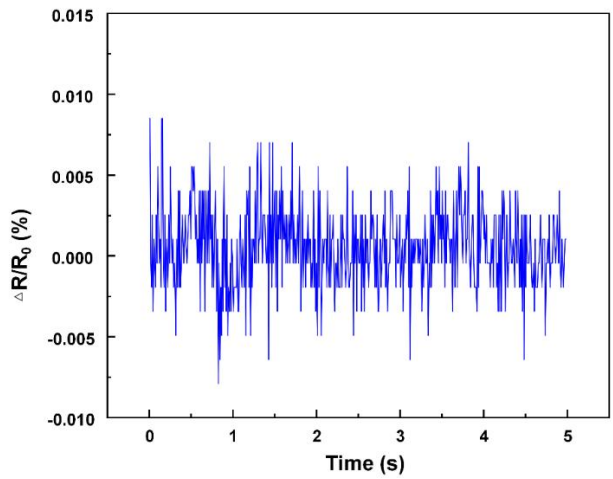

Supplementary Figure 14. The raw resistance change collected over 5 seconds with no applied bending.

Supplementary Text 8. Long-term stability and environmental durability evaluation.

1. Sensitivity stability

Two groups of 14-day experiments were carried out to assess sensitivity under varying conditions. In the first group, relative humidity (RH) was fixed at 70%, while temperature was varied from 25 °C to 55 °C. At 25 °C, wrist extension (W-E), wrist flexion (W-F), and finger bending (F-B) all maintained the highest sensitivity with variations below 5%. Sensitivity gradually decreased with rising temperature, yet it remained above 90% of the initial value after 14 days, indicating good thermal stability. In the second group, temperature was held at 25 °C while humidity was varied between 70% RH and 20% RH. Sensitivity was optimal at 70% RH and declined with decreasing humidity due to reduced hydrogel water content. Even at 20% RH, sensitivity remained at a relatively high level after 14 days, ensuring reliable performance in dry environments. The corresponding results are summarized in Figures 15 and 16.

2. Hysteresis robustness

Long-term hysteresis tests were also performed for 14 days. With humidity fixed at 70% RH and temperatures ranging from 25 °C to 55 °C, the hysteresis ratio was initially 4–5% and increased slightly with temperature, remaining below 10% at 55 °C. With temperature fixed at 25 °C and humidity varied from 70% RH to 20% RH, hysteresis stability was best at 70% RH and rose moderately at lower humidity due to gradual hydrogel dehydration. Even under 20% RH, the hysteresis ratio remained below 12% after 14 days. These results demonstrate that hysteresis is minimal and stable under standard conditions, and remains well controlled in harsher environments due to the double-network hydrogel structure. The corresponding results are summarized in Figures 17 and 18.

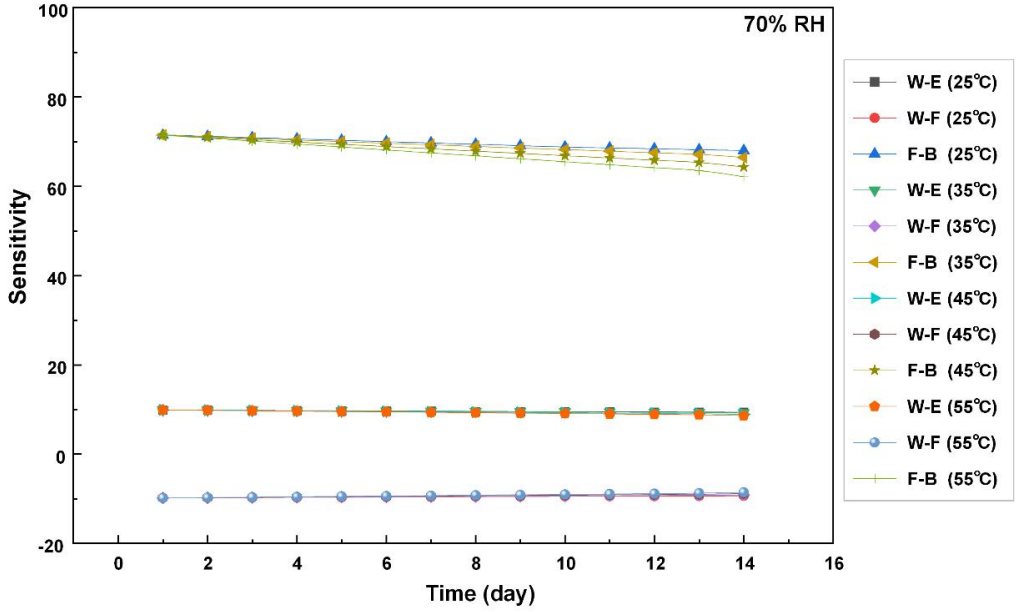

Supplementary Figure 15. Sensitivity variation over 14 days under different temperatures at 70% RH.

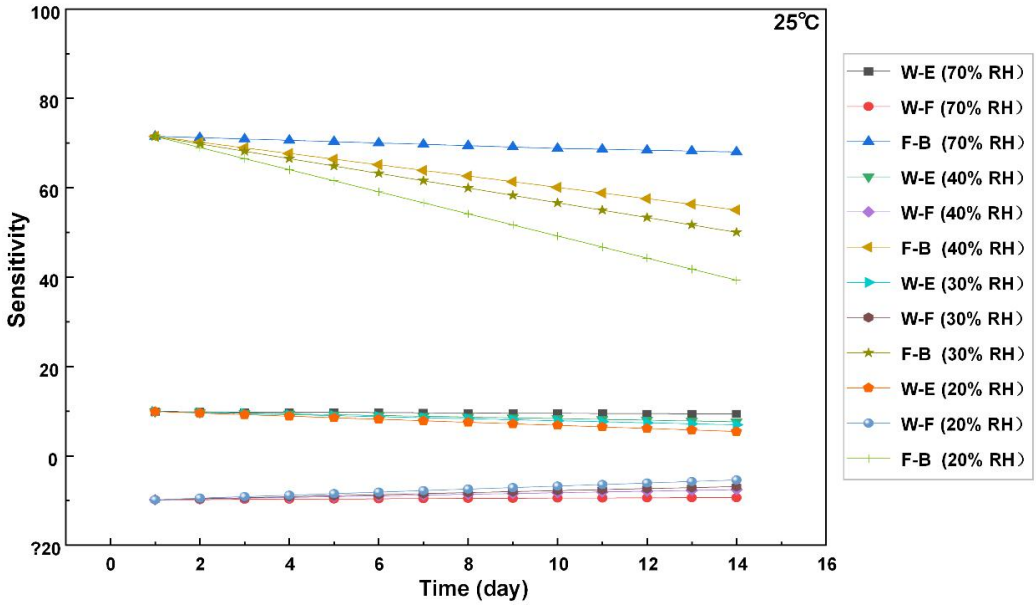

Supplementary Figure 16. Sensitivity variation over 14 days under different humidity levels at 25 °C.

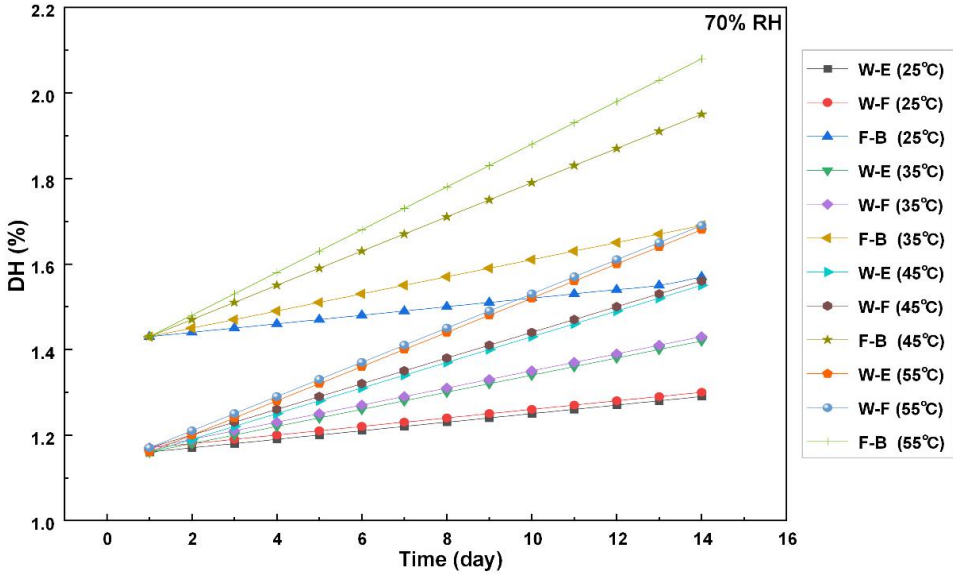

Supplementary Figure 17. Hysteresis ratio variation over 14 days under different temperatures at 70% RH.

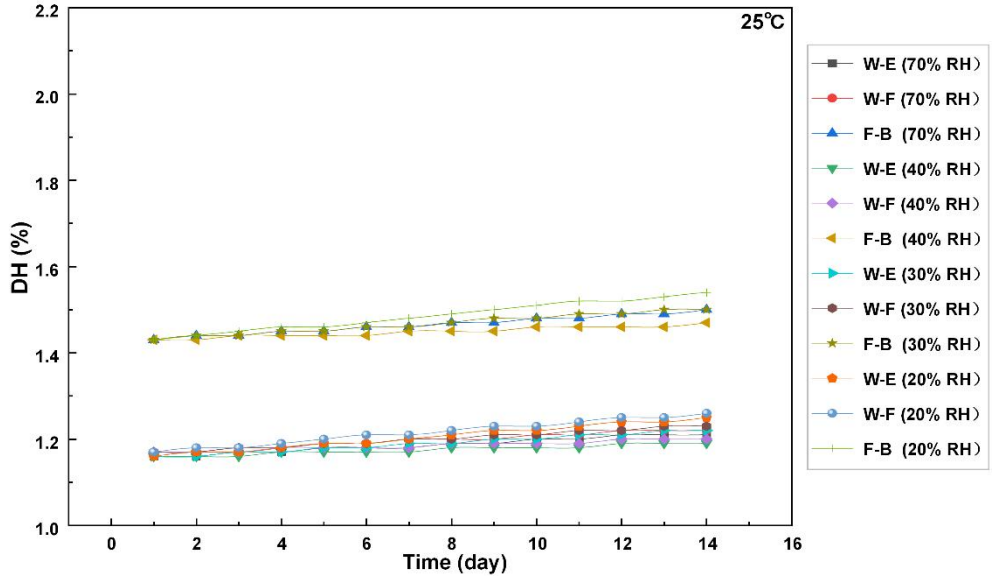

Supplementary Figure 18. Hysteresis ratio variation over 14 days under different humidity levels at 25 °C.

Supplementary Text 9. Stability of hydrogel-based finger bending sensors in dry environments.

The reproducibility of the hydrogel strain sensor was systematically evaluated under two RH levels (30% and 70%) during a 10,000-s cyclic test, with finger flexion and extension applied every 10 s. As shown in Figure 19, the sensor exhibits stable and reproducible responses across all humidity conditions. At higher humidity (70% RH), the hydrogel maintains excellent elasticity and ionic conductivity, yielding highly consistent signals with minimal drift (Figure 19A). At relatively dry humidity (30% RH), the sensor maintained stable output, with only a slight decrease in $\Delta R/R_0$ amplitude, indicating that the hydrogel preserves its functional integrity (Figure 19B).

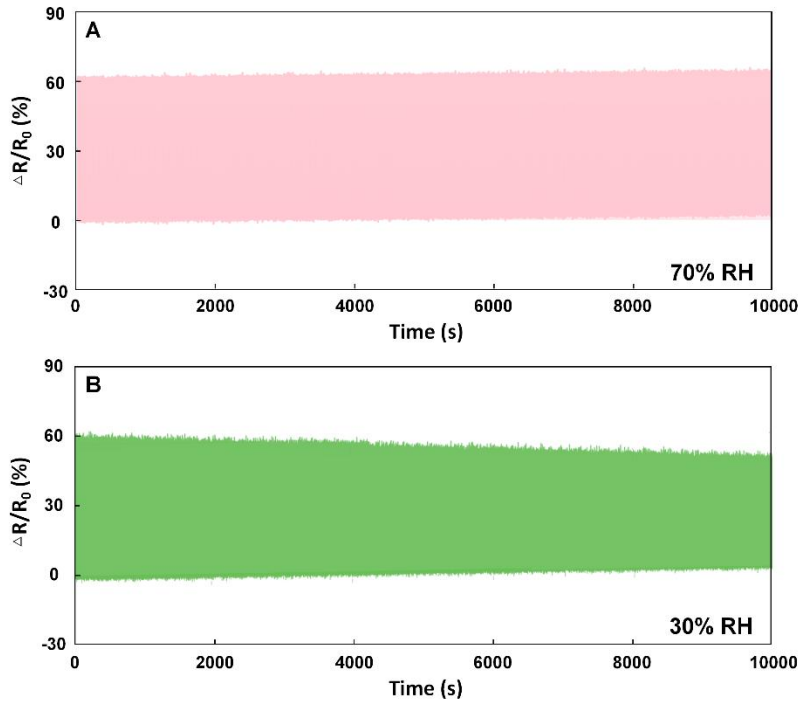

Supplementary Figure 19. Repetitive bending tests of Finger-fiber under different humidity conditions. (A) Test performed at 70% RH; (B) Test performed at 30% RH.

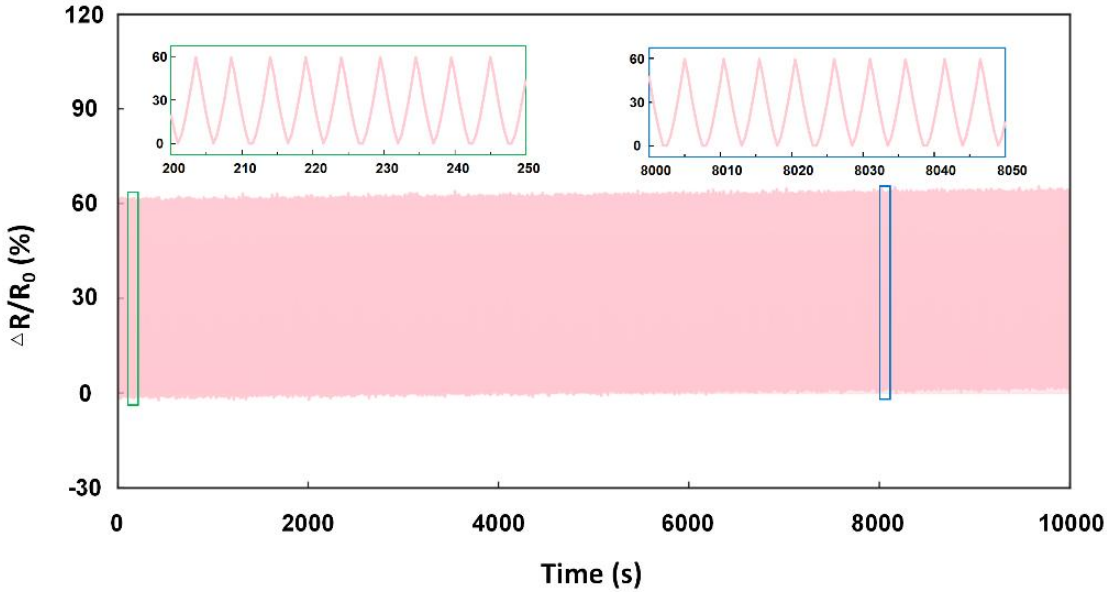

Supplementary Figure 20. Reproducibility and long-term durability of the Finger-fiber.

Supplementary Table 4. Comparison between representative studies and the Touch-Code Glove.

Work	Focus	Mechanism/ Interface	Key performance	Form factor	Relation to our work
[1]	Atomically ultraflat graphene on mica	Materials platform (atomic flatness)	Surface roughness ~24–25 pm	Material/substrate	Provides material foundation, not HRI system
[2]	Graphene heterodyne vapor sensing	Conductance modulation + high-frequency mixing	Sensitivity ~0.64 ppb; response ~0.1 s	Single sensor	Breakthrough in chemical sensing, not interactive control
[3]	Multi-receptor e-skin (tele- + tactile perception)	Structured nanoparticle doping, field enhancement	$\Delta V/\Delta d$ = 14.2; classification accuracy 99.56%; inference 0.0439 s	E-skin array	Focus on non-contact perception & array benchmarks, not wearable glove
Our work	Multimodal wearable HRI glove	Triboelectric digital encoding + hydrogel strain + CNN-LSTM	Gesture/touch recognition >98 %; stable real-time control	Wearable glove system	Emphasizes system-level integration & real-time HRI; complementary to prior works

REFERENCES

[1] Nature 462, 339–341 (2009)

[2] Nature Communications 5, 4376 (2014)

[3] Science Advances 10 (37), eadp8681

Supplementary Text 10. Structural framework for 1D-CNN.

To enable robust recognition of multi-finger gestures from multi-channel strain signals, a 1D convolutional neural network (1D-CNN) is constructed, as illustrated in Figure 21. The network receives an input tensor of size 5×200, representing five parallel signal channels corresponding to five fingers over 200 time steps. The convolutional front-end comprises four sequential 1D convolutional layers with increasing channel depths of 16, 32, 64, and 128, respectively. Each convolutional layer adopts a kernel size of 3 and a stride of 1, combined with a "same" padding scheme to maintain the temporal resolution across layers.

To progressively downsample the temporal dimension and emphasize hierarchical feature learning, max-pooling layers with a pooling size of 2 are interleaved after the first three convolutional blocks, while the final pooling operation uses average pooling. After the final convolutional stage, the output feature map is flattened into a one-dimensional vector and passed to a fully connected dense network for classification. The dense layers capture high-level representations and produce gesture predictions via a softmax classifier. This architecture enables efficient local feature extraction across temporal scales and is well-suited for precise gesture recognition under individual variability in glove usage.

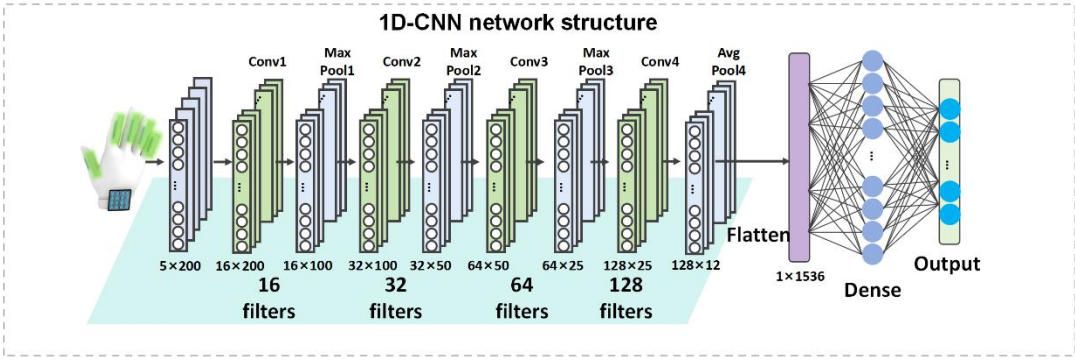

Supplementary Figure 21. Structural framework for 1D-CNN.

Supplementary Table 5. Parameters of the 1D-CNN structure.

Network layer	Parameter	Activation function	Output size
Input	/	/	5×200
Conv1	Kernel size = 3, Stride = 1, Filters = 16, Padding = same	ReLU	16×200
Max Pool1	Pooling size = 2	/	16×100
Conv2	Kernel size = 3, Stride = 1, Filters = 32, Padding = same	ReLU	32×100
Max Pool2	Pooling size = 2	/	32×50
Conv3	Kernel size = 3, Stride = 1, Filters = 64, Padding = same	ReLU	64×50
Max Pool3	Pooling size = 2	/	64×25
Conv4	Kernel size = 3, Stride = 1, Filters = 128, Padding = same	ReLU	128×25
Avg Pool4	Pooling size = 2	/	128×12
Flatten	/	/	1×1536
Dense Layer 1	Weight = 1536×128	ReLU	128
Dense Layer 2	Weight =128×10	ReLU	10

Supplementary Text 11. Multi-user generalization of CNN-LSTM and 1D-CNN models.

To evaluate cross-user generalization, experiments were conducted with 10 volunteers (ages 22-35 years, palm widths 15-21 cm) to cover representative variability in hand geometry and gesture habits.

1. CNN-LSTM model

For triboelectric signal decoding, each subject provided 50 samples per mode across four modes, resulting in 2,000 triboelectric samples. As shown in Table 6 and Figure 22, classification accuracies across the four modes ranged from 91.6% to 96.0%, with an average of 93.5%. Accuracy remained consistently above 91%, indicating robustness to inter-user variability. Mode 2 reached the highest accuracy (96.0%), while most misclassifications occurred between Mode 1 and Mode 3, which share similar temporal-spatial contact dynamics.

2. 1D-CNN model

For strain-based gesture recognition, each subject performed 20 samples per mode across 10 gesture classes, yielding 2000 strain samples. Results in Table 7 and Figure 23 show accuracies between 80.0% and 96.5%, with an average above 90%. Gesture 7 achieved the highest accuracy (96.5%), while Gestures 6 (80.0%) and 10 (85.0%) showed lower performance due to higher intra-class variability and overlap in strain patterns. Despite modest decreases, the model maintained stable recognition across participants, confirming reliable generalization.

Overall, both CNN-LSTM and 1D-CNN models demonstrated strong robustness under multi-user conditions, ensuring reliable recognition performance across diverse users.

Supplementary Table 6. Classification accuracies for different modes using the new multi-user testing dataset.

Mode category	Mode 1	Mode 2	Mode 3	Mode 4
Classification accuracy (%)	91.6	96.0	92.0	94.4

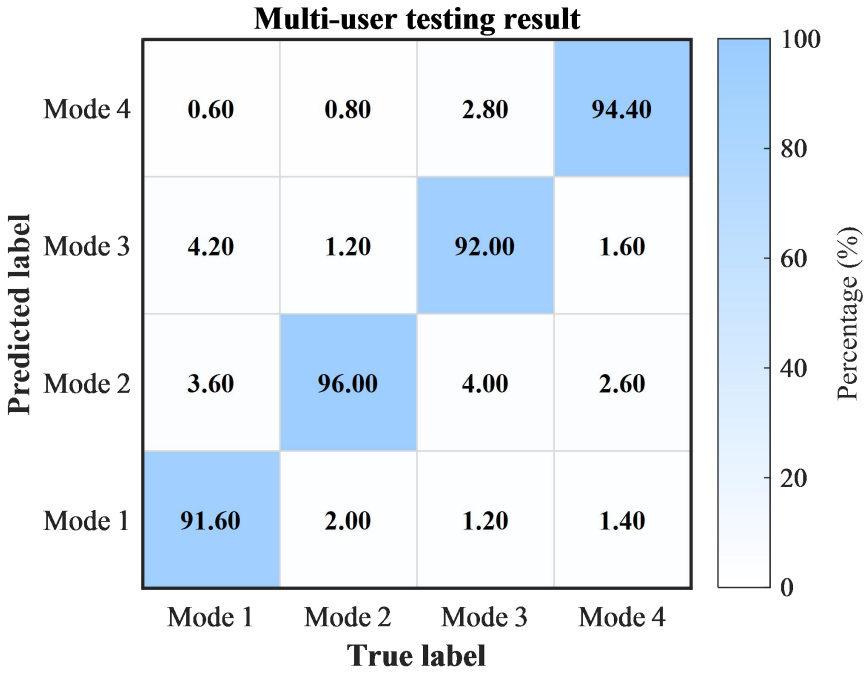

Supplementary Figure 22. Confusion matrices of classification results using the new multi-user testing dataset.

Supplementary Table 7. Classification accuracies of different gestures using the new multi-user testing dataset.

Gesture category	Gesture 1	Gesture 2	Gesture 3	Gesture 4	Gesture 5
Classification accuracy	89.5	94.5	90.5	91.5	89.5
Mode category	Gesture 6	Gesture 7	Gesture 8	Gesture 9	Gesture 10
Classification accuracy	80.0	96.5	92.0	92.5	85.0

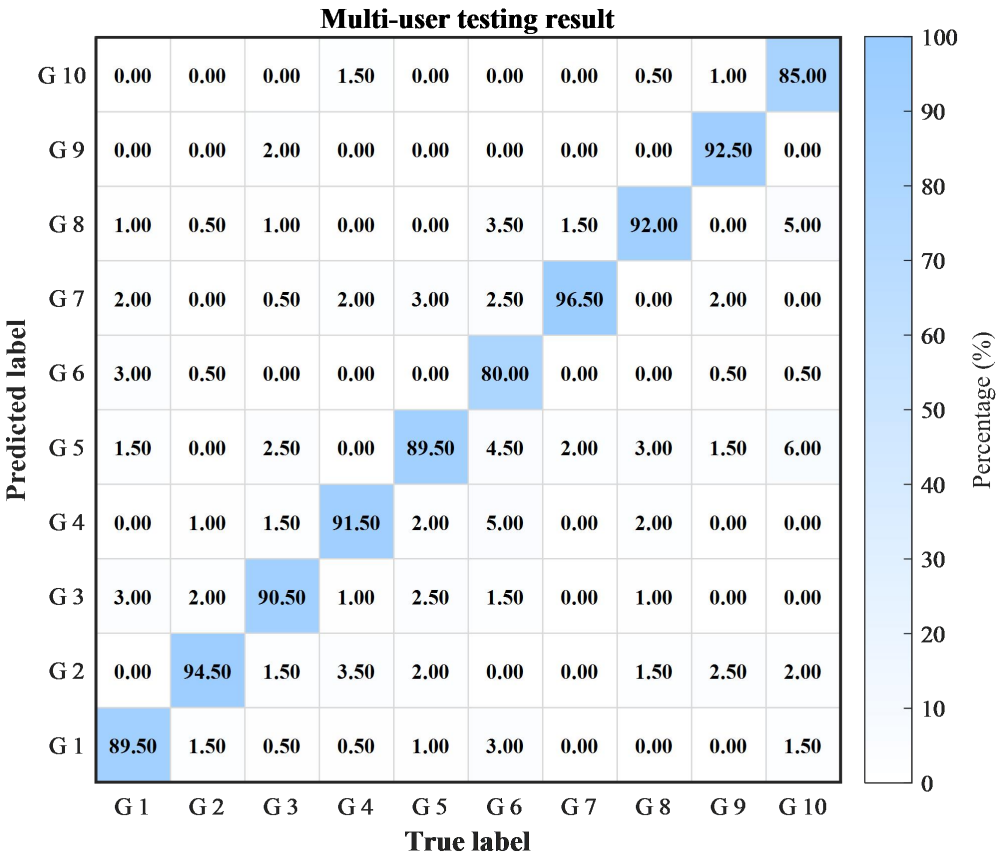

Supplementary Figure 23. Confusion matrices of classification results using the new multi-user testing dataset. “G” indicates “gesture”.

Supplementary Text 12. Touch-to-path mapping strategy based on triboelectric touch inputs.

To enable intuitive path control of the robotic arm, triboelectric touch gestures on the Wrist-pad were mapped to specific spatial motions. As shown in Figure 24A(i), when the user sequentially touches the points P14-P10-P6-P2 along the second column of the Wrist-pad, a forward translation of the robotic arm is triggered. Conversely, touching the points in reverse order, P2-P6-P10-P14, initiates a backward movement. These commands drive coordinated rotations of the robotic arm's three primary joints while keeping the end-effector's orientation stable, resulting in a horizontal displacement without any angular deviation of the robotic hand. Similarly, Figure 24A(ii) illustrates lateral translation control through touch gestures along the second row of the Wrist-pad. A rightward path is generated by the sequence P5-P6-P7-P8, and a leftward motion is achieved by the reverse order P8-P7-P6-P5. This interaction adjusts two main joints to induce side-to-side translation while maintaining the hand's horizontal alignment and posture. In both cases, the number of activated points directly determines the duration of the arm's movement.

Furthermore, Figure 24B demonstrates advanced gesture-based programming. The user performs a composite touch sequence following the pattern P9-P5-P6-P7-P8-P12, which forms an inverted-U shape on the Wrist-pad. This gesture is translated into a corresponding spatial path, where the robotic hand follows a smooth arc resembling an inverted U in three-dimensional space. This is achieved through dedicated joint control logic that maps the geometric shape of the touch input to the physical path of the robot, showcasing the system's ability to interpret complex input patterns for customized path generation.

In terms of command editing, since the wrist-pad contains only four sensing points in each row and column, long sliding commands require a specific strategy for handling prolonged pressing. As shown in Figure 25A, the triboelectric sensor generates a complete waveform for each contact-release cycle, regardless of the interval between contact and separation. Dynamic regions (yellow) correspond to touch and release events, while static regions (green) indicate intervals without movement. Even during extended pressing, the release event consistently produces a clear dynamic signal, ensuring that no information is lost.

To achieve continuous control of the robotic arm, a sliding-pressing mechanism was introduced in the wrist-pad. When the finger sequentially touches three sensing points, a long press on the fourth point maintains the previous command; once the press ends and the finger is lifted, a release signal is immediately generated, serving as a termination command to stop the arm. Figure 25B and 25C illustrates this strategy in the P5-P8 regions of the 4×4 array, where three stages can be clearly distinguished: dynamic response during touch, stable output during keeping, and a final dynamic response during move (release).

These results demonstrate that the system remains robust under prolonged pressing conditions and provides clear and reliable control logic.

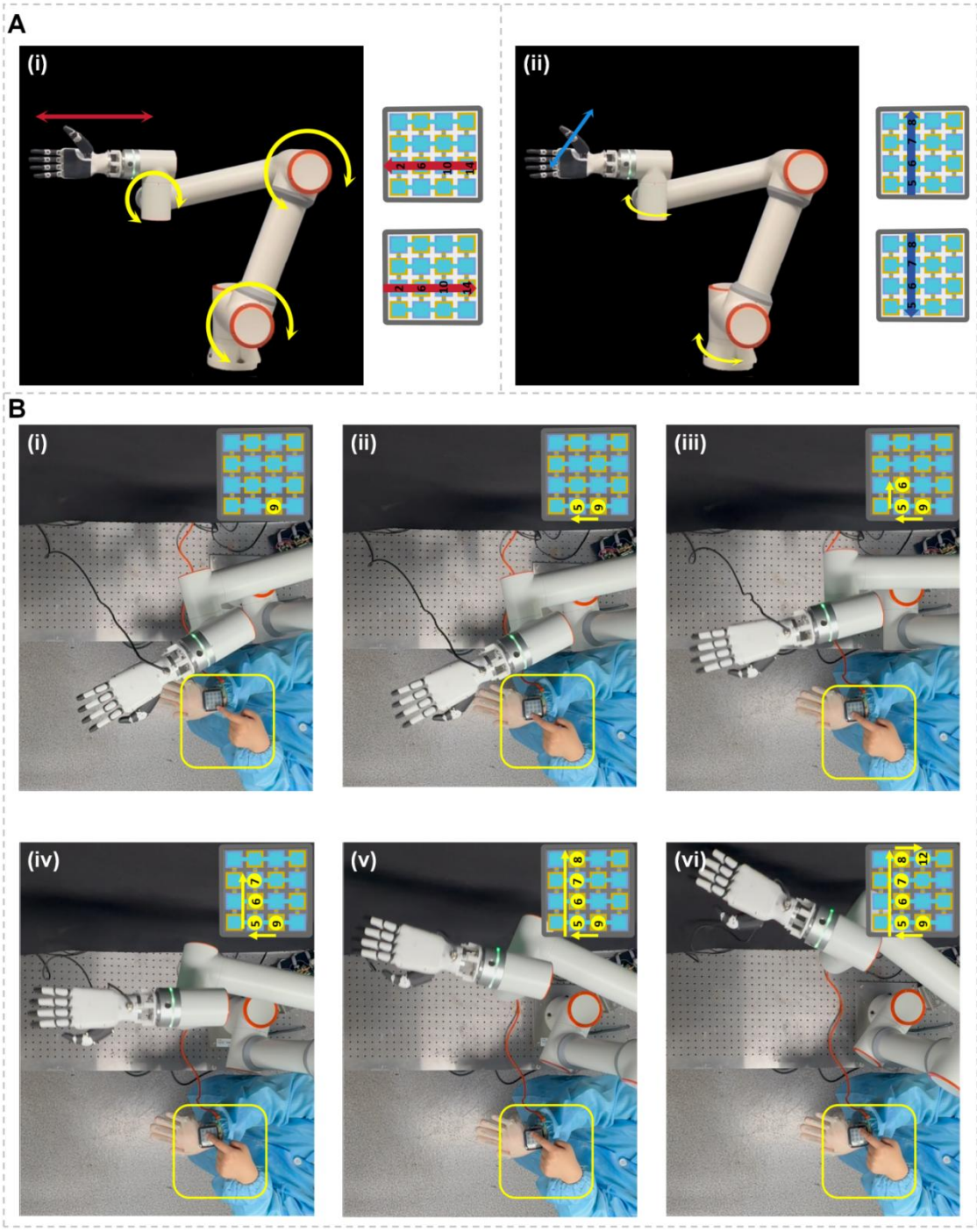

Supplementary Figure 24. Touch-based path programming via triboelectric touch commands on the Wrist-pad. (A) Schematic diagrams illustrating gesture-based control strategies for robotic arm translation; (B) Experimental demonstration of a complex gesture input (P9-P5-P6-P7-P8-P12) forming an inverted-U pattern, mapped to a spatially smooth arc path of the robotic arm through customized joint control.

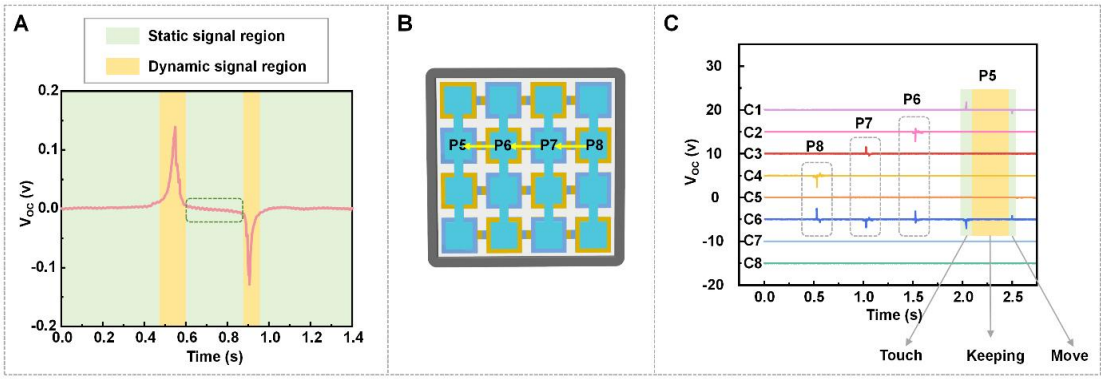

Supplementary Figure 25. Response of the triboelectric wrist-pad under prolonged pressing and sequential gestures. (A) Schematic illustration of dynamic and static regions of the triboelectric signal; (B) Touch command sequence; (C) Recorded triboelectric signal waveforms.

Supplementary Text 13. Signal acquisition circuitry for strain and triboelectric sensing in the Touch-Code glove.

Figure 26 presents the circuit designs used for acquiring both resistive and triboelectric signals. Figure 26A and Figure 26B show the circuits designed for capturing strain signals from finger and wrist bending. Figure 26A illustrates the basic voltage divider circuit employed during calibration experiments. A series resistor is introduced to limit the voltage applied across the hydrogel, thereby preventing electrolysis or degradation that could alter its internal resistance and compromise signal accuracy. Figure 26B depicts an improved version of the strain signal acquisition circuit, incorporating an operational amplifier and a low-pass filter to enhance signal stability and robustness. The principle of strain signal amplification is as follows: the circuit essentially functions as a low-pass filter and comprises three parts, as shown in the schematic. The first part (highlighted in yellow) provides a constant input voltage to the hydrogel electrode. The second part (in green) includes an operational amplifier configured to ensure that the current passing through the amplifier's feedback resistors R_1 and R_2 equals the current through the hydrogel resistor ($R_{hydrogel}$). The third part (in pink) consists of two resistors, R_1 and R_2, and a capacitor. R_1 and the capacitor form a filter to suppress high-frequency interference such as electromagnetic noise, while R_2 is an adjustable resistor used to fine-tune the current to match varying hydrogel resistances. The output voltage, representing the final measured signal, is the sum of the voltage drops across R_1 and R_2. This configuration reliably converts the resistance signal from the hydrogel-based sensor into a stable voltage output, making it well-suited for downstream robotic control tasks. Figure 26C shows a commercial signal conditioning module for triboelectric signal acquisition. This integrated module features both amplification and filtering stages, enabling the system to reliably detect the characteristic voltage waveforms generated during triboelectric interactions and ensuring high signal integrity throughout subsequent processing and control.

To verify that the circuit integrated with the Touch-Code Glove can ensure normal signal acquisition under environmental electrical noise or static interference, a dual hardware strategy was implemented. A high-performance filtering circuit module was adopted to suppress environmental noise and static interference. As shown in Figure 27A, the circuit module is presented, and its function is to effectively suppress background noise and stabilize the output. Figure 27B illustrates the raw output signals

without any circuit, which exhibit strong noise interference. By contrast, Figure 27C shows the signals after introducing the filtering circuit, where the noise is significantly reduced and the triboelectric waveforms become clearly distinguishable.

These results confirm that the filtering circuit alone is sufficient to effectively suppress environmental electrical noise and static interference, thereby ensuring reliable signal acquisition and stable operation of the glove system in practical environments.

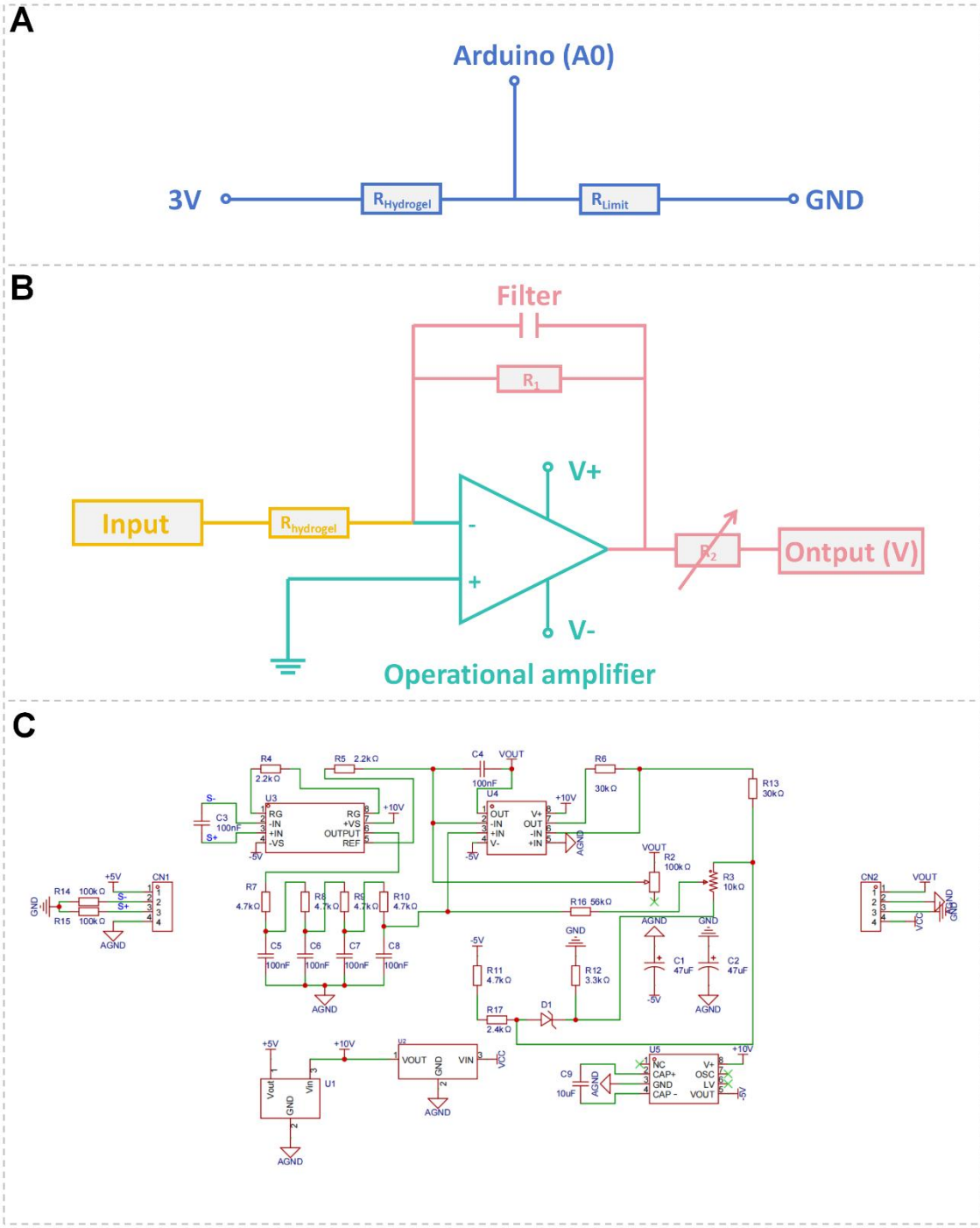

Supplementary Figure 26. Signal acquisition circuits for resistive and triboelectric sensing. (A) Calibration circuit for hydrogel-based strain sensing using a voltage divider; (B) Amplification and filtering circuit with operational amplifier for stable strain signal output; (C) Commercial module for triboelectric signal acquisition and conditioning.

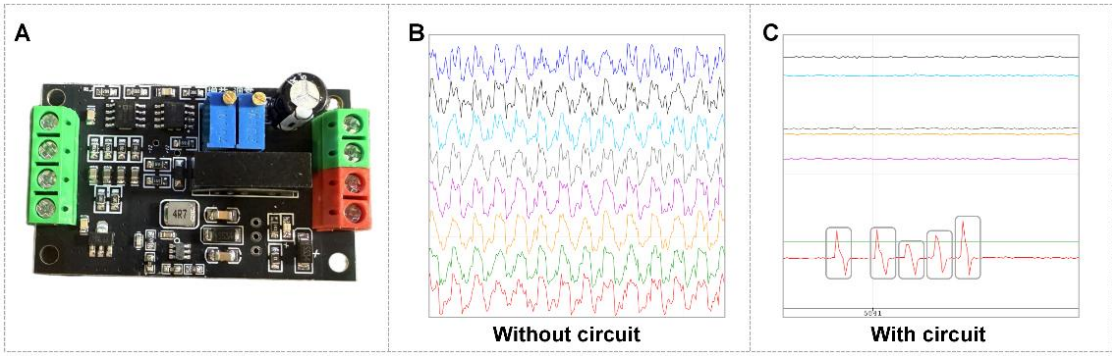

Supplementary Figure 27. Verification of noise suppression for the Touch-Code Glove. (A) Photograph of the signal acquisition circuit; (B) Raw triboelectric signals without circuit conditioning; (C) Triboelectric signals after circuit conditioning.

Supplementary Text 14. Ergonomic evaluation of the glove prototype.

The glove prototype has a weight of 36.8 g and is fabricated from silicone rubber, providing good flexibility and electrical insulation. As shown in Figure 28, the glove can be stretched from 20.5 cm to 43.7 cm, corresponding to a maximum strain of 113.2%, which demonstrates high mechanical flexibility.

To assess ergonomic performance in long-term use, an 8-hour continuous wearing test was conducted under summer indoor conditions, comparing the optimized glove with a commercial silicone glove. As illustrated in Figure 29A, the commercial glove showed poor breathability, resulting in fingertip skin peeling after prolonged wear. In contrast, the optimized glove incorporating a thin moisturizing inner layer preserved both comfort and skin integrity. Figure 29B further shows that only mild sweat accumulation occurred between 2 PM and 3 PM, likely due to peak ambient temperature, while no fingertip peeling appeared during the entire 8-hour test.

These results confirm that the silicone-based glove prototype can be worn comfortably for extended sessions when optimized, providing a basis for further exploration of lightweight and breathable materials to enhance ergonomic performance.

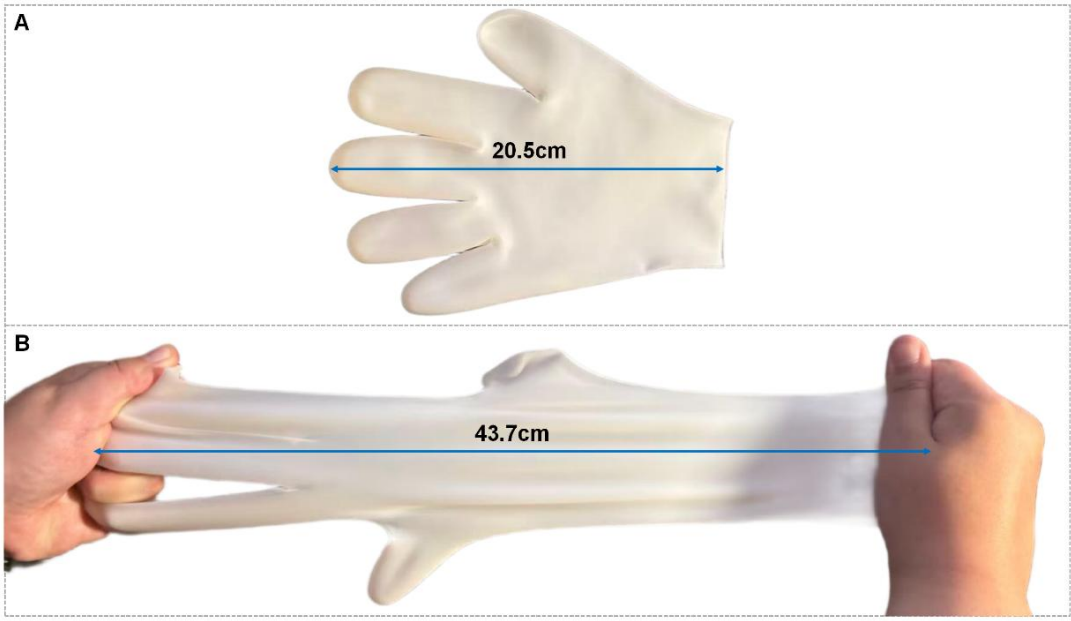

Supplementary Figure 28. Mechanical flexibility of the glove prototype. (A) Glove prototype before stretching; (B) Glove prototype after stretching.

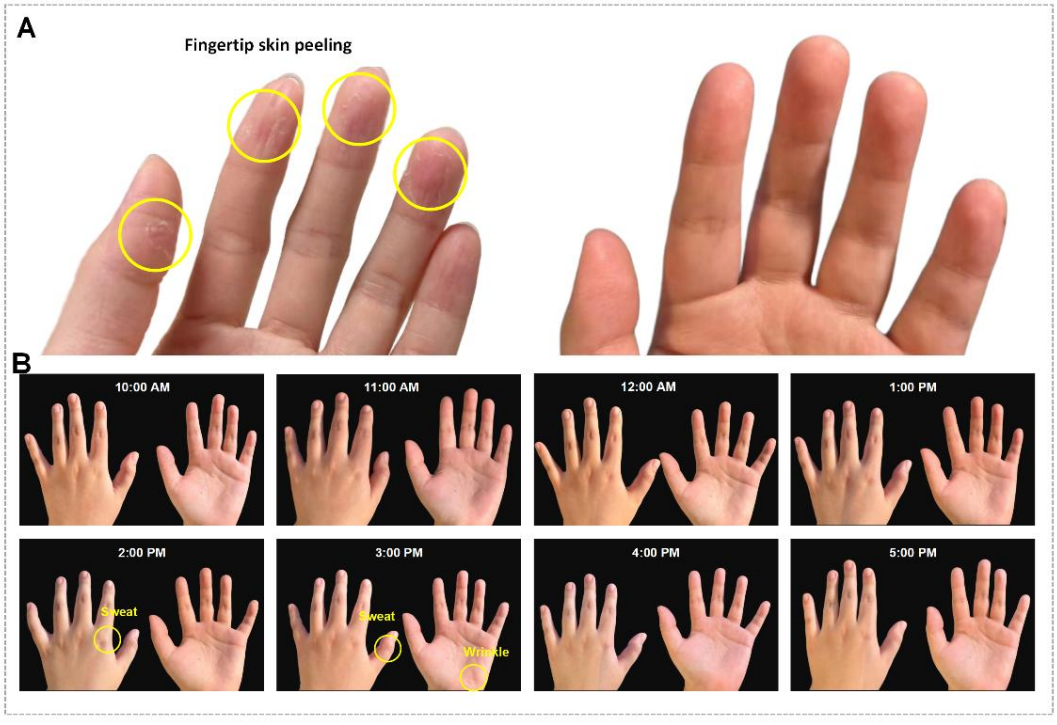

Supplementary Figure 29. Ergonomic performance during long-term wearing. (A) Comparison of finger crease formation; (B) Demonstration of the glove's long-term wearing breathability.